High-Performance Supercapacitor Applications of NiO-Nanoparticle-Decorated Millimeter-Long Vertically Aligned Carbon Nanotube Arrays via an Effective Supercritical CO_2-Assisted Method

Junye Cheng, Bin Zhao, Wenkang Zhang, Feng Shi, Guangping Zheng, Deqing Zhang, and Junhe Yang**

Nickel oxide (NiO) nanoparticles are distributed uniformly in the vertically aligned carbon nanotube arrays (VACNTs) with millimeter thickness by an effective supercritical carbon dioxide-assisted method. The as-prepared VACNT/NiO hybrid structures are used as electrodes without binders and conducting additives for supercapacitor applications. Due to the synergetic effects of NiO and VACNTs with nanoporous structures and parallel 1D conductive paths for electrons, the supercapacitors exhibit a high capacitance of 1088.44 F g^{-1}. Furthermore, an asymmetric supercapacitor is assembled using the as-synthesized VACNTs/NiO hybrids as the positive electrode and the VACNTs as the negative electrode. Remarkably, the energy density of the asymmetric supercapacitor is as high as 90.9 Wh kg^{-1} at 3.2 kW kg^{-1} and the maximum power density reaches 25.6 kW kg^{-1} at 24.9 Wh kg^{-1}, which are superior to those of the NiO or VACNTs-based asymmetric supercapacitors. More importantly, the asymmetric supercapacitors exhibit capacitance retention of 87.1% after 2000 cycles at 5 A g^{-1}. The work provides a novel approach in decorating highly dense and long VACNTs with active materials, which are promising electrodes for supercapacitors with ultrahigh power density and energy density.

1. Introduction

In recent years, the ever-increasing demand for energy and growing concerns on air pollution and global warming have stimulated much research in developing effective energy conversion and storage systems for alternative energy sources. Supercapacitors, including electric double-layer capacitors (EDLCs) and pseudocapacitors, are considered as promising charge storage devices owing to their fast charge and discharge rates, long life cycle, and low maintenance cost.[1–3] The design of electrode materials therein is of scientific and engineering significances since the electrodes are vital to the supercapacitors with superior electrochemical performance.

3D carbon-based nanostructures, in particular the vertically aligned carbon nanotube arrays (VACNTs), could be an ideal architecture for electrode materials because of their large specific surface areas,[4] high conductivity,[5] and excellent chemical stability.[6] In CNT arrays, each individual CNT can be considered as a nanoscale electrode whose orientation is consistent with each other, promoting the motions of electrons along the same direction to form well-orientated 1D conductive paths.[7] Moreover, the appropriate intertube spacing among CNTs can ensure the highly efficient transport of electrolytic ions and intermediate reactants.[8] However, the electrical double-layer capacitance made of VACNTs alone could not lead to electrochemical supercapacitors with satisfactory performance. Alternatively, pseudocapacitors have higher energy densities than those of EDLCs, since their capacitances are mainly attributed to the continuous and reversible redox reactions of electroactive species of the electrode materials, such as surface functional groups and transition metal oxides (TMOs).[9] But there are also obvious drawbacks of these TMOs, including low electric conductivity, poor rate performance, and limited cycling ability.[9] Therefore, in order to develop high-performance supercapacitors, TMOs should be uniformly introduced on surfaces of nanotubes

J. Cheng
School of Energy and Power Engineering
University of Shanghai for Science and Technology
Shanghai 200093, China
Prof. B. Zhao, W. Zhang, Prof. J. Yang
School of Materials Science and Engineering
University of Shanghai for Science and Technology
Shanghai 200093, China
E-mail: zhaobin@usst.edu.cn; jhyang@usst.edu.cn
F. Shi, Prof. D. Zhang
Key Laboratory of Fine Chemicals
College of Heilongjiang Province
Qiqihar University
Qiqihar 161006, China
Prof. G. Zheng
Department of Mechanical Engineering and Shenzhen Research Institute
Hong Kong Polytechnic University
Hung Hom, Kowloon, Hong Kong, China

DOI: 10.1002/adfm.201502711

within VACNTs to construct composite structure of the electrode materials.

There are some practical constraints in the preparation of VACNTs/TMOs. First, due to the nanoscaled intertube spacing of VACNTs, especially those of the highly dense, millimeter-long carbon nanotube arrays, it is difficult to uniformly decorate TMOs on CNT surfaces. Second, millimeter-long VACNTs as the support for pseudocapacitors is advantageous since the power density and energy density of supercapacitor cells increase with increasing weight of the active materials occupied on the surfaces of carbon nanotubes.[10,11] However, treatment of VACNTs with TMOs is still an issue yet to be resolved and there are few reports on the functionalization of VACNTs with a thickness above 1000 μm to date. Third, the hydrophobic property of VACNTs has prevented the aqueous solution from entering the spaces inside VACNTs, leading to the difficulties in the synthesis of VACNTs/TMOs from inorganic aqueous reactions.[12] Fourth, organic reagents are also not suitable for the synthesis of VACNTs/TMOs since VACNTs are liable to collapse and agglomerate when contacting with organic reagents directly.[5,6] To tackle the above-mentioned restrictions, in the past decade, different methods have been developed to fabricate TMO-decorated VACNTs. One of the most widely reported methods is the electrochemical deposition, which is employed to fabricate VACNTs/nickel oxide (NiO),[13] VACNTs/MnO_2,[14] VACNTs/CoO_x,[15] etc. Nevertheless, limitations of the electrochemical deposition technique are significant. For example, the parameters for electrochemical deposition have to be tuned precisely;[16] the aligned structure of VACNTs may be damaged[17] and the deposition of TMOs only reaches micrometer level below the top surface of VACNTs.[18] Recently a new strategy involving nebulized ethanol assisted infiltration has been developed to fabricate 3D structure-based VACNTs uniformly decorated with TMOs.[7] Although various TMOs can be uniformly decorated in VACNTs, this method is not necessarily viable in decorating highly dense, millimeter-long VACNTs. Although it has been found that[10] Mn_3O_4 nanoparticles can be homogenously deposited within dense VACNTs from nonaqueous solutions via a dip-casting method, the electrochemical performance of the composite is unsatisfactory. Hence, it is still a challenging task to obtain 3D structure-based VACNTs/TMOs hybrid structures with desirable electrochemical performances.[19–22]

In this study, to address the aforementioned issues, we develop an effective supercritical carbon dioxide ($SCCO_2$) assisted method in uniformly decorating highly dense, millimeter-long VACNTs with NiO nanoparticles. Nickel oxide has been demonstrated as a promising electrode material because of its excellent pseudocapacitive properties, environmental-friendly characteristic and lower cost compared to other metal oxides such as MoO_3, MnO_2, and Co_3O_4.[23–26] In addition, the supercritical CO_2 used in the preparation of VACNTs/NiO has some advantages such as the accessible supercritical conditions (i.e., 31 °C and 7.38 MPa), low cost, nonflammability, and nontoxicity. The most important motivation of using $SCCO_2$ comes from its excellent penetration ability, near-zero surface tension, low viscosity, and strong solvent capability, which readily delivers a high density of reactants and promotes a high uniformity and conformal coverage of complex surfaces. Moreover, the great wettability of $SCCO_2$ to the hydrophobic surfaces of VACNTs results in the intimate contact between VACNTs and the electrolyte.[27] To the best of our knowledge, the synthesis of VACNTs/NiO hybrid structures using the $SCCO_2$ technique has not been reported in the literature. As illustrated in **Scheme 1**, the routine of synthesis can be described as three simple steps, as follows. First, the highly dense, millimeter-long VACNTs are synthesized by the water-assisted chemical vapor deposition (CVD). The image of VACNTs is shown in Figure S1a in the Supporting Information. The number density of CNTs in the VACNTs is adjusted by varying the thickness of iron catalyst layer used in the CVD process. Second, the benzene solution containing the nickelocene is filled into the spaces inside VACNTs with the aid of $SCCO_2$, resulting in the VACNTs/nickelocene systems as shown in Scheme 1. The photo of $SCCO_2$ processed VACNTs is shown in Figure S1b in the Supporting Information. Third, the VACNTs/nickelocene system is annealed to obtain VACNTs decorated with nickel oxide nanoparticles. It is noted that this strategy can also be extended to integrate other metal oxide nanoparticles, or even metallic nanoparticles (by annealing in reducing environments), into VACNTs for different applications. Our study shows that the VACNTs/NiO hybrids can achieve a high capacitance of 1088.44 F g^{-1}. Furthermore, the VACNTs/NiO hybrid materials can be used to assemble asymmetric pseudocapacitors which exhibit a superior overall performance of high capacitance, high energy density at high power density and long cycling life time.

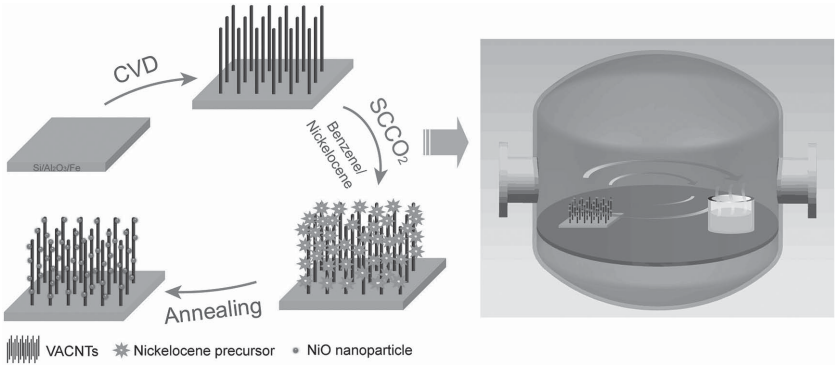

Scheme 1. Left) Schematic illustration of the synthesis of the VACNTs/NiO hybrid structure and right) schematic of $SCCO_2$ processing of VACNTs in the pressure vessel.

2. Results and Discussion

2.1. Morphology and Structural Characterizations

In the preparation of VACNTs/NiO, particular emphasis is given to the selection of appropriate organic solvents as the intermediate phase, which can well dissolve nickelocene precursor and can be easily dissolved in supercritical CO_2. Different organic solvents such as alcohol, acetone, and benzene were employed to investigate the weight of nickelocene gained in the VACNTs after the supercritical CO_2 treatment. As listed in Table S1 in

the Supporting Information, the pure VACNTs obtained the maximum gain of nickelocene when benzene was used as the solvent. And the gained weight was almost twice as much as that of VACNTs using alcohol or acetone as the solvent. This can be explained by the fact that benzene has good miscibility with CO_2 because of its nonpolar feature and that nickelocene is more soluble in benzene than alcohol or acetone.[28] Because the dissolving capacity of $SCCO_2$ fluid is very sensitive to the change of temperature or pressure in the vessel, and the small increase in pressure often leads to higher solubility of $SCCO_2$ fluid.[29] Therefore, we also investigate the effects of pressure on the weight of nickelocene gained in VACNTs. Interestingly, it is observed that the weight of nickelocene gained in VACNTs does not increase with the increasing $SCCO_2$ pressure in the vessel, as listed in Table S2 in the Supporting Information. Thus, it is speculated that the increase in pressure only promotes the solubility of benzene in supercritical CO_2 but does not improve the solubility of nickelocene in benzene.

The morphology of the pure VACNTs and VACNTs/NiO hybrids were examined by field emission scanning electron microscopy (FESEM) as shown in Figure S2 in the Supporting Information and **Figure 1**, respectively. Figure S2a,c (Supporting Information) shows that the pure VACNTs possess vertically aligned structures and are highly dense. The aligned pores or channels in VACNTs are indicated by the arrows in Figure S1b,d, in the Supporting Information which are advantageous to ions diffusion and the electrochemical performance of electrode materials. In our previous work, the individual CNT within the as-grown VACNTs was proved to have an average diameter of ≈7 nm with a CNT wall number of 2–6.[30,31] The height and density of the VACNTs was

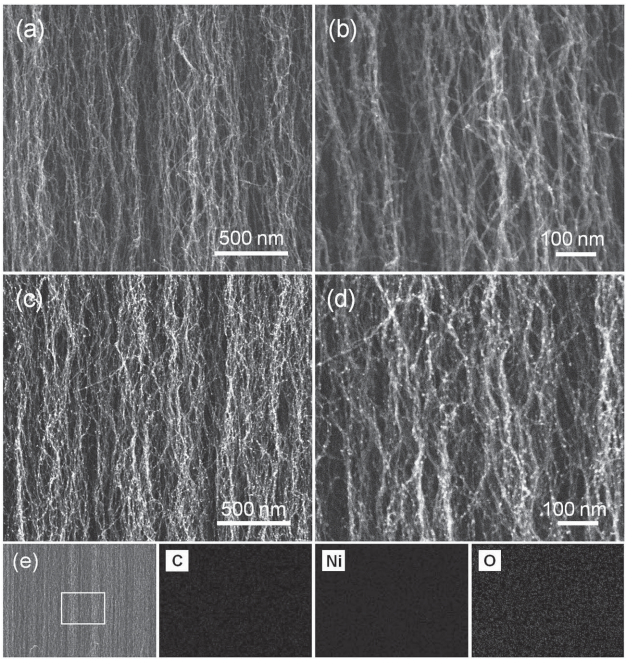

Figure 1. FESEM images of cross sections of VACNTs/NiO hybrids at different magnifications. a,b) VN-19.3 sample. c,d) VN-43.4 sample. e) Cross-sectional SEM image of VN-43.4 sample and its corresponding EDS mapping patterns for C, Ni, and O elements.

1.18 mm and 3.1 mg cm^{-2}, respectively.[30] Figure 1a–d shows the SEM images showing the cross sections of VACNTs/NiO hybrids with two different weight percentages of NiO after 6 h annealing of the VACNTs/nickelocene samples at 350 °C, respectively. The annealing temperature is determined from the thermogravimetric analysis (TGA) shown in Figure S3 in the Supporting Information. Note that we obtained two different weight percentages of nickel oxide for VACNTs/NiO (19.3 and 43.4 wt%) with the VACNTs fabricated with the same growth conditions. The specimens are denoted as VN-*x* where *x* stands for the weight percentage of NiO. Figure 1a,b shows the SEM images showing the cross sections of VN-19.3 sample. Uniformly distributed nanoparticles can be clearly observed, especially in Figure 1b. Figure 1c,d shows the SEM images of VN-43.4 sample. Both images show that nanoparticles are homogeneously distributed in the VACNT arrays. The uniform distribution of nanoparticles inside the sample (VN-43.4) is confirmed by energy dispersive spectrometer (EDS) mapping, as shown in Figure 1e. Various elements (carbon, nickel, and oxygen) are found to distribute uniformly throughout the VACNTs. This can be attributed to the advantages of the $SCCO_2$ processing method. The gas-like diffusivity, the high-penetration ability, and zero surface tension of $SCCO_2$ lead to rapid delivery of the precursors and uniformly coverage of the CNT walls in the highly dense, millimeter-long VACNT arrays, thereby allowing TMOs to be distributed uniformly in VACNTs. The results described above thus prove that the $SCCO_2$-assisted method in uniformly decorating highly dense, millimeter-long VACNTs is viable and effective.

As shown in **Figure 2**a, element analysis on the selected red area in Figure 1e using the EDS reveals that the as-obtained hybrids contain nickel, carbon, and oxygen. The calculated atomic ratio of Ni to O is close to 1, which preliminarily confirms that the nanoparticles embedded in the VACNTs are NiO. Figure 2b shows the typical X-ray diffraction (XRD) patterns of the pure VACNTs and as-obtained hybrids. Clearly, the peaks at 37.2°, 43.4°, 62.8°, 75.5°, and 79.8° could be observed, which are indexed as (111), (200), (220), (311), and (222) crystal planes of the NiO phase (JCPDS No. 04-0835) respectively, in excellent agreement with the reported values.[32–34] It is noteworthy that the characteristic peaks of VN-43.4 sample are stronger than those of VN-19.3, which is attributed to the increase of NiO contents in VN-43.4. No additional peaks apart from those of VACNTs and NiO are observed, indicating that high-purity NiO nanoparticles are obtained during the synthesis process. The oxidation states of transition-metal elements in the VN-43.4 samples are studied by X-ray photoelectron spectroscopy (XPS), as shown in Figure 2c,d. The XPS spectrum for Ni 2p shown in Figure 2c is found to possess two satellites (marked as "Sat.") close to two spin–orbit doublets at 874.7 and 856.8 eV respectively, indicating the presence of Ni^{2+}.[35] As shown in Figure 2d, the peak at 529.8 eV can be assigned to O 1s of NiO.[36] Since high weight percentage of nickelocene in VACNTs/nickelocene could be oxidized completely, the relatively low contents of nickelocene in VACNTs/nickelocene would certainly be oxidized. These results reveal that the nickelocene has been transformed to NiO nanoparticles in the millimeter-long VACNTs annealed at 350 °C for 6 h.

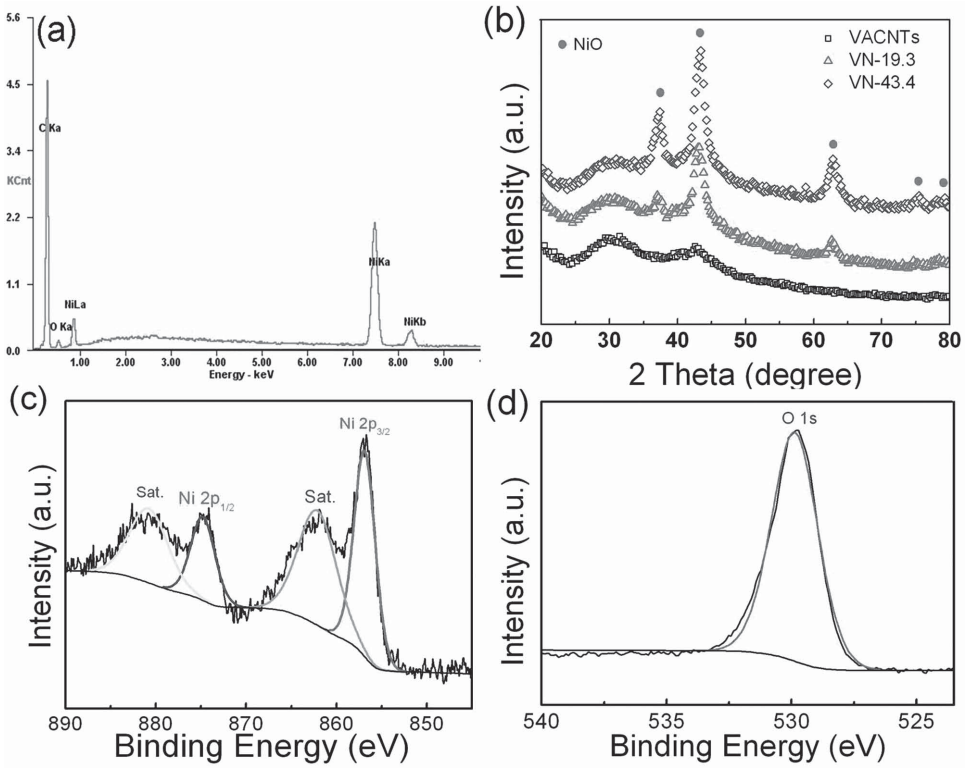

Figure 2. a) Selected-area (rectangle in Figure 1e) EDS spectrum of VN-43.4 sample. b) XRD patterns of VACNTs, VN-19.3, and VN-43.4 samples. c) Ni 2p, and d) O 1s XPS spectra of VN-43.4 sample.

Transmission electron microscopy (TEM) and high resolution TEM (HRTEM) were employed to further investigate the morphology and microstructure of as-obtained samples. The results are shown in **Figure 3**. Figure 3a,b are TEM images of VN-19.3 sample at different magnifications. It is clearly shown that the CNT walls are rough due to the decorated NiO nanoparticles. These nanoparticles are uniformly dispersed along the CNTs and the average particle size of NiO is ≈10 nm. Compared to the VN-19.3 sample, VN-43.4 sample possesses more NiO nanoparticles while they still homogeneously distribute (Figure 3c,d) along the CNTs. Thus the TEM images further confirm the effectiveness of $SCCO_2$-assisted method in preparing high-quality VACNTs/NiO. In addition, it is noted that the NiO nanoparticles in VN-43.4 sample are smaller than those in VN-19.3 samples and the average size is ≈5 nm. The small sizes of NiO nanoparticles in VN-43.4 sample could result from the intense interactions among Ni precursors in the limited free spaces inside VACNTs during the annealing process because of the high contents (71.3 wt%) of nickelocene in VACNTs/nickelocene. The HRTEM image of a single NiO nanoparticle and its corresponding fast Fourier transform (FFT) pattern are shown in Figure 3e and f, respectively. Two kinds of lattice planes can be clearly observed in Figure 3e and the distances of the adjacent lattice planes are about 0.208 nm and 0.210 nm, which correspond to those of (200) and $(0\bar{2}0)$ planes of cubic NiO, respectively. The FFT pattern suggests that the (200), $(2\bar{2}0)$ and $(0\bar{2}0)$ planes of cubic NiO under the incident electron beam are along the $[00\bar{4}]$ direction.

2.2. Electrochemical Properties of VACNTs/NiO Hybrid Materials

Cyclic voltammetry (CV) and galvanostatic charge–discharge (GCD) techniques were employed to investigate the electrochemical behaviors of the VACNTs/NiO hybrid materials used as electrodes of supercapacitors. For comparison, electrochemical behaviors of pure VACNTs were investigated. As shown in Figure S4a (Supporting Information), the nearly rectangular shape of CV curves with no obvious redox peaks from 0 and 0.6 V indicates good double-layer capacitive performance of the VACNTs electrode at different scan rates. The highest specific capacitance of 105 F g^{-1} is obtained for the VACNTs electrode at a scan rate of 5 mV s^{-1}. This value is higher than the previously reported results obtained in aqueous and organic solutions for VACNTs with different heights.[37–39] **Figure 4**a,c shows typical CV curves of VACNTs/NiO hybrid material electrodes in a 6 M KOH electrolyte at different scan rates between 0 and 0.6 V. Obviously, two strong symmetrical redox peaks appear in the VACNTs/NiO hybrid material electrodes at different scan rates. Because large redox current peaks are observed only under Faradaic reaction, it is suggested that the obtained peak capacitance is mainly derived from the surface Faradaic reaction, which can be expressed as [40]

$$NiO + OH^- \leftrightarrows NiOOH + e^- \quad (1)$$

The symmetry of redox peaks reveals the reversibility of the electrode reaction. The galvanostatic charging–discharging

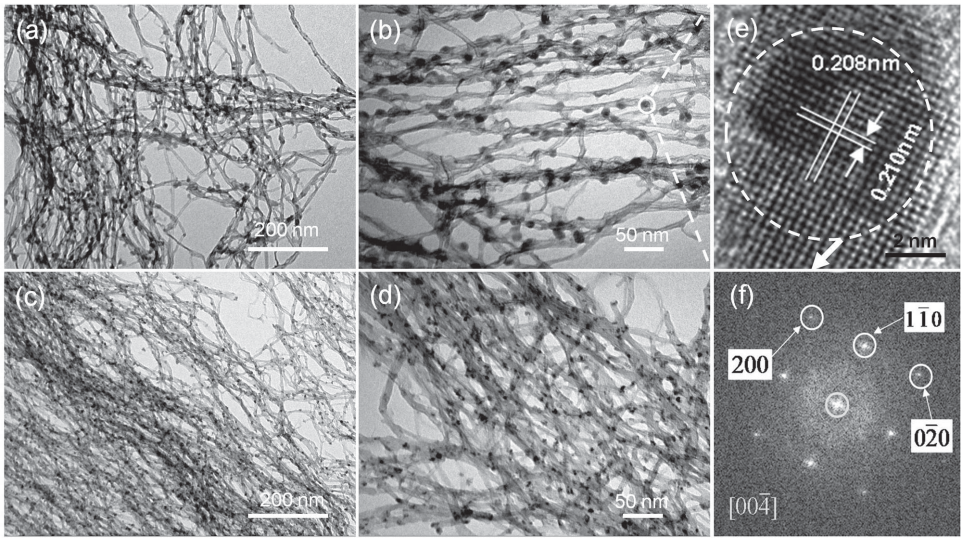

Figure 3. a,b) TEM images of VN-19.3 at different magnifications. c,d) TEM images of VN-43.4 at different magnifications. e) HRTEM image of NiO nanoparticle in VN-19.3. f) FFT pattern of the selected area in image (e).

was carried out to further evaluate the electrochemical performance of the VACNTs/NiO hybrids. Figure 4b,d shows the nonlinear voltage–time profiles for the electrodes at different current densities, which are quite different with that of the conventional double-layer capacitors. The results demonstrate the existence of the Faradaic reactions, in consistent with the CV results.[38,39] The calculated specific capacitances (C_s) for the VN-43.4 and VN-19.3 hybrid structure electrodes are presented in Figure 4e. The specific capacitances of VN-19.3 electrode are 543.06, 325.07, 225.21, 156.23, 122.41, and 95.61 F g^{-1} at scan rates of 5, 10, 20, 50, 100, and 200 mV s^{-1}, respectively. Because of its higher loading of NiO, the VN-43.4 electrode exhibits higher C_s values (1088.44, 748.58, 576.96, 431.495, 261.59, and 163.84 F g^{-1} at scan rates of 5, 10, 20, 50, 100, and 200 mV s^{-1}, respectively) than those of the VN-19.3 electrode. It can be also found that the specific capacitance decreases gradually with increasing scan rate. At a low scan rate, electrolytic ions can diffuse and migrate into active materials. At a high scan rate, on the contrary, the diffusion and migration of electrolytic ions are restricted, leading to the disability of the inner active surface area for charge storage. The maximum C_s (1088.44 F g^{-1} at 5 mV s^{-1}) is significantly higher than the previously reported specific capacitances of VACNT-based hybrid materials and even other NiO-based hybrid materials. For comparison, Table S3 in the Supporting Information lists the electrochemical performances of the previously reported VAVNT-based and NiO-based supercapacitors. Figure 4f shows the Nyquist plots for the two composite electrodes analyzed by electrochemical impedance spectroscopy (EIS). The impedance spectra consist of two branches, i.e., a depressed semicircle in the high-frequency region which is usually called Warburg semicircle and a straight line in the low-frequency region which corresponds to ion diffusion in the electrode material.[41] As shown in Figure 4f, the low-frequency straight line of the VN-43.4 sample is almost vertical, indicating its better capacitive behavior compared with that of VN-19.3 sample. The result is consistent with the CV and GCD results described above. Another important parameter, the intrinsic resistance of electrodes in the high-frequency region (also called Faraday resistance), determines charging and discharging rates of supercapacitors and is an extremely significant factor that affects the power density of a supercapacitor. The intrinsic resistance values obtained from the *x*-intercept of the Nyquist plots are measured to be 5.5 and 3.2 Ω for VN-43.4 and VN-19.3 samples, respectively. This trend may be attributed to a larger quantity of nonconductive NiO nanoparticles for VN-43.4 sample which have been observed in the TEM images shown in Figure 3c,d.

The reasons for the ultrahigh specific capacitance of the VACNTs/NiO hybrid materials can be explained as follows. First, the unique nanostructured features of VACNTs/NiO hybrid structures consisting of the highly dense and long VACNTs and embedded NiO nanoparticles with uniform morphology and good crystallinity play a key role in the electrochemical performance. In particular, the aligned hydrophilic nanoporous channels of VACNTs (Figure S1b,d, Supporting Information) and the uniformly distributed NiO nanoparticles could provide paths for fast electrolyte ion diffusion into the hybrid arrays and quick Faradaic reactions. Second, the VACNTs/NiO hybrid materials are directly used as electrodes without any binders and conducting additives, eliminating extra contact resistance or weight. Moreover, because each NiO nanoparticle is connected directly with the CNTs, the spontaneous electron transfer between CNTs and NiO occurs.[42] Thus, the "electron superhighways" of CNTs and uniformly distributed NiO form a superior conducting network, which allows for efficient charge transport and enhances the electronic conductivity of the composite significantly. Third, CNTs and the decorated NiO is a framework with exceptional mechanical properties which could solve the cyclic degradation problems caused by mechanical deformation or volume changes. Therefore, the VACNTs/NiO hybrid material electrodes exhibit the superior electrochemical capacitive performance, as shown in Figure 4.

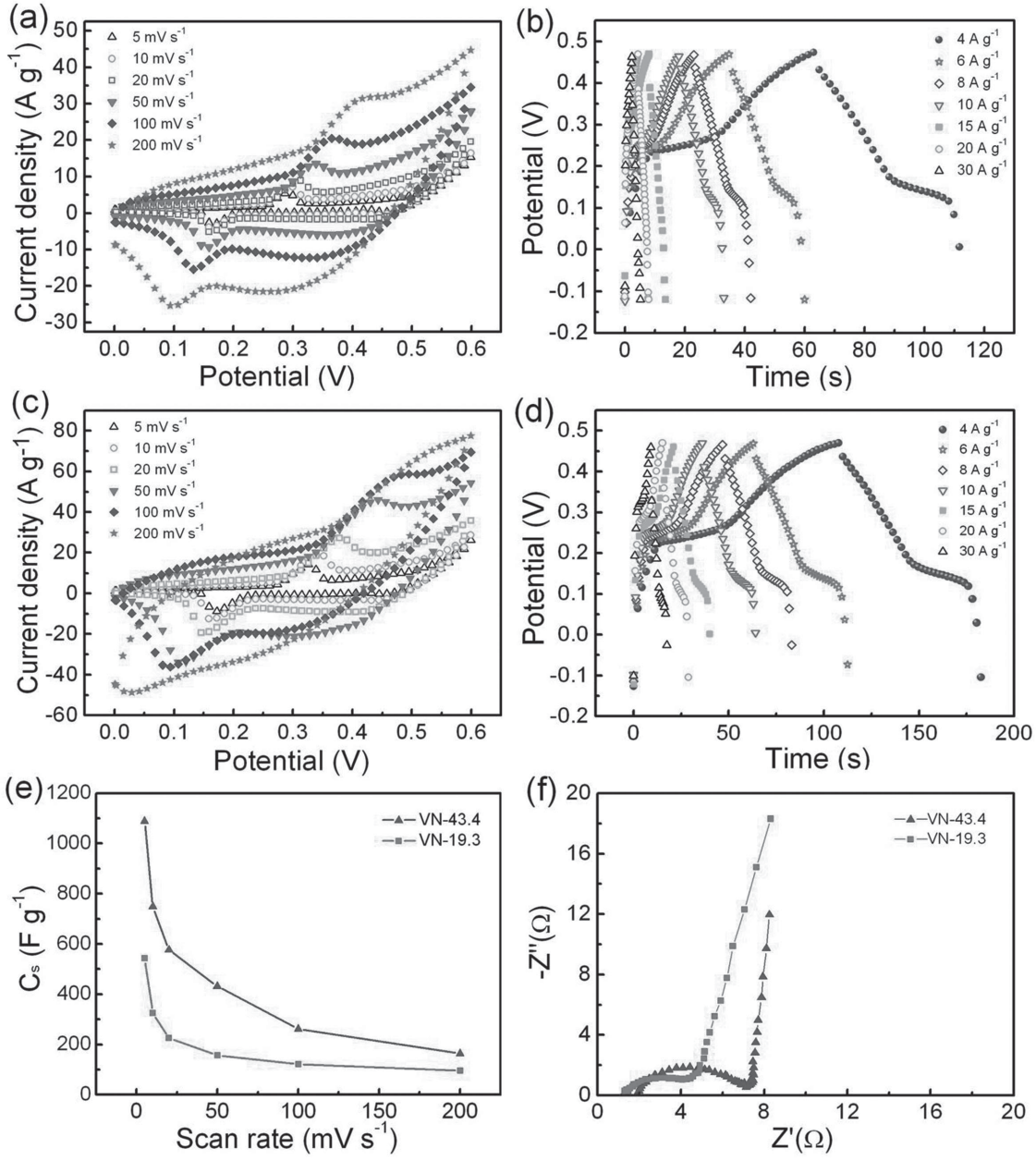

Figure 4. a) Cyclic voltammograms of VN-19.3 samples at different scan rates in 6 M KOH. b) Galvanostatic charge–discharge curves of VN-19.3 sample at different current densities. c) Cyclic voltammograms of VN-43.4 sample at different scan rates in 6 M KOH. d) Galvanostatic charge–discharge curves of VN-43.4 sample at different current densities. e) Specific capacitance for the VN-43.4 and VN-19.3 hybrid material electrodes at various scan rates. f) Nyquist plots for VN-43.4 and VN-19.3 hybrid material electrodes.

2.3. The Effects of Annealing Temperature on the Capacitive Performance

The morphology of nickel oxide and the electrochemical capacitive performance of the composites are usually determined by the annealing conditions in the preparation of the VACNTs/NiO hybrids. Here, we investigate the effects of annealing temperature on the resulting VACNTs/NiO hybrid structures. **Figure 5** shows the TEM results of two VACNTs/nickelocene (Vn) samples containing 44.7 and 71.3 wt% nickelocene precursors after annealing at different temperatures (325, 350, and 375 °C) for 6 h, which are denoted as Vn-44.7–325 °C, Vn-44.7–350 °C, Vn-44.7–375 °C, Vn-71.3–325 °C, Vn-71.3–350 °C, and Vn-71.3–375 °C, respectively. It is found that the size of nanoparticles increases and then decreases with increasing annealing temperature for the VACNTs/nickelocene samples with low nickelocene loading (44.7 wt%). Furthermore, the Vn-44.7–325 °C sample has inhomogeneous particle size distribution, which might be caused by the incomplete oxidation according to the XPS results shown in Figure S5 in the Supporting Information. It has been found that there are some residue nickelocene in the Vn-44.7–325 °C sample. When the

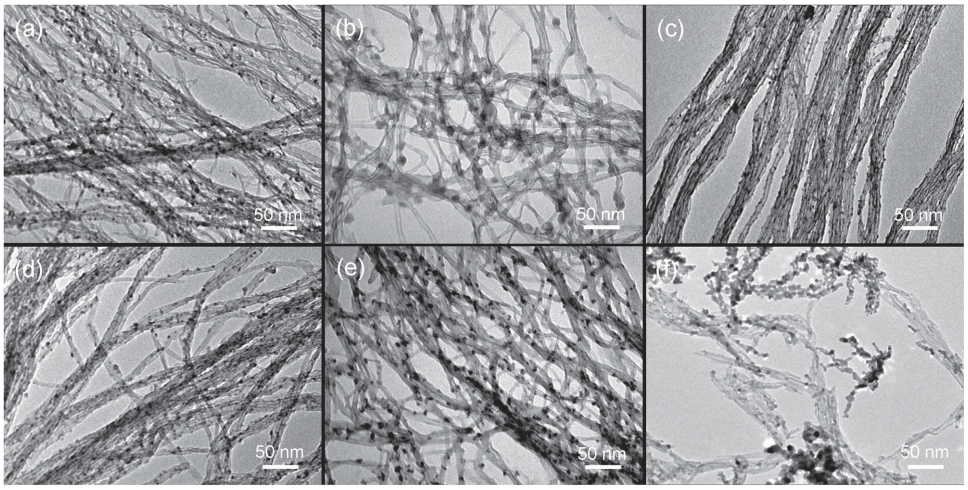

Figure 5. TEM images of a) Vn-44.7–325 °C, b) Vn-44.7–350 °C, c) Vn-44.7–375 °C, d) Vn-71.3–325 °C, e) Vn-71.3–350 °C, and f) Vn-71.3–375 °C samples.

annealing temperature is increased to 350 °C, the complete oxidization of nickelocene into NiO could occur. For the Vn-44.7–375 °C sample, tiny NiO nanoparticles homogeneously coated on the CNT walls can be observed (Figure 5c). Interestingly, there are no large-sized nanoparticles for the VACNTs/nickelocene samples with high nickelocene loading (71.3 wt%) and some NiO nanoparticles agglomerate and disperse heterogeneously in the Vn-71.3–375 °C samples (Figure 5f). The morphology of NiO nanoparticles in the Vn-71.3–350 °C sample could be mainly associated with the limited free spaces of the VACNTs. It can be concluded that the appropriate annealing temperatures for Vn samples with 44.7 and 71.3 wt% nickelocene are 375 and 350 °C, respectively.

Figure 6 shows the electrochemical capacitive performance of Vn-44.7 and Vn-71.3 samples annealed at different temperatures (325, 350, and 375 °C). From the CV curves at a scan rate of 5 mV s^{-1} for the Vn-44.7 samples (Figure 6a), it can be found that the sample annealed at 375 °C exhibits the largest loop area, indicating its superior capacitive performance. Figure 6b shows the GCD curves (at 2 A g^{-1}) for Vn-44.7 samples annealed at different temperatures. The sample annealed at 375 °C exhibits the longest discharge time, representing the highest specific capacitance in agreement with the CV results. The specific capacitances calculated from the GCD curves for the Vn-44.7 samples annealed at 325, 350, and 375 °C are 303.3, 314.67, and 350.7 F g^{-1} at a current density of 2 A g^{-1}, respectively. It is noted that the specific capacitance increases with increasing annealing temperature. Based on the XPS results (Figure S5, Supporting Information), the lowest specific capacitance for sample annealed at 325 °C could result from the incomplete oxidation of nickelocene.[43–46] On the contrary, the Vn-44.7 sample annealed at 375 °C achieves the highest specific capacitance. The reason is that the annealing of Vn-44.7 samples with less nickelocene loading results in smaller sizes of nickel oxide as shown in Figure 5c. Thus, the distance over which the electrolyte ions must transport is shortened, leading to more effective use of electrode materials and thus a higher specific capacitance.[10] Figure 6c shows the CV curves of the Vn-71.3 samples annealed at different temperatures. All samples exhibit a pair of oxidation/reduction peaks at a scan rate of 5 mV s^{-1}. But the two redox peaks are weak for the Vn-71.3–375 °C sample. As shown in Figure 5f, since NiO nanoparticles severely agglomerate in Vn-71.3–375 °C samples, the relatively weak oxidation/reduction reaction could occur. Figure 6d shows the galvanostatic charge–discharge curves (at 2 A g^{-1}) for the Vn-71.3 samples annealed at different temperatures. Among the three samples, the one annealed at 350 °C exhibits the longest discharge time, and the samples annealed at 325 °C have the shortest discharge time. The calculated specific capacitances are 385.56, 631.17, and 573.83 F g^{-1} for Vn-71.3 samples annealed at 325, 350, and 375 °C, respectively. It is thus concluded that annealing of Vn-71.3 samples with more nickelocene loading at 350 °C leads to the highest specific capacitance.

The long-term cycling stability is usually required for the practical applications of supercapacitors. The Vn-44.7–350 and Vn-71.3–350 °C electrodes are subjected to an extensive charge–discharge cycling at 30 A g^{-1} and the results are depicted in Figure 6e and f, respectively. A slight increase of specific capacitance at the initial stage of cycling can be observed in the curves, which suggests an activation process.[47] After 1000 cycles, 93.2% and 89.3% of specific capacitances are reserved for the Vn-44.7–350 °C and Vn-71.3–350 °C electrodes, respectively, indicating that the VACNTs/NiO electrodes possess excellent cycle stability. Such outstanding electrochemical performances demonstrate that the VACNTs/NiO hybrids can be promising candidate for supercapacitors.

2.4. Overall Electrochemical Performance of VACNT/NiO-Based Asymmetric Supercapacitor

To further evaluate the capacitive performances of the as-prepared VACNTs/NiO hybrids, we choose the Vn-71.3–350 °C samples which have the best capacitive performance in the three-electrode testing as the positive electrode and pure VACNTs as the negative electrode to construct a three-electrode asymmetric supercapacitor, as shown in **Figure 7**a. Figure 7b shows the CV

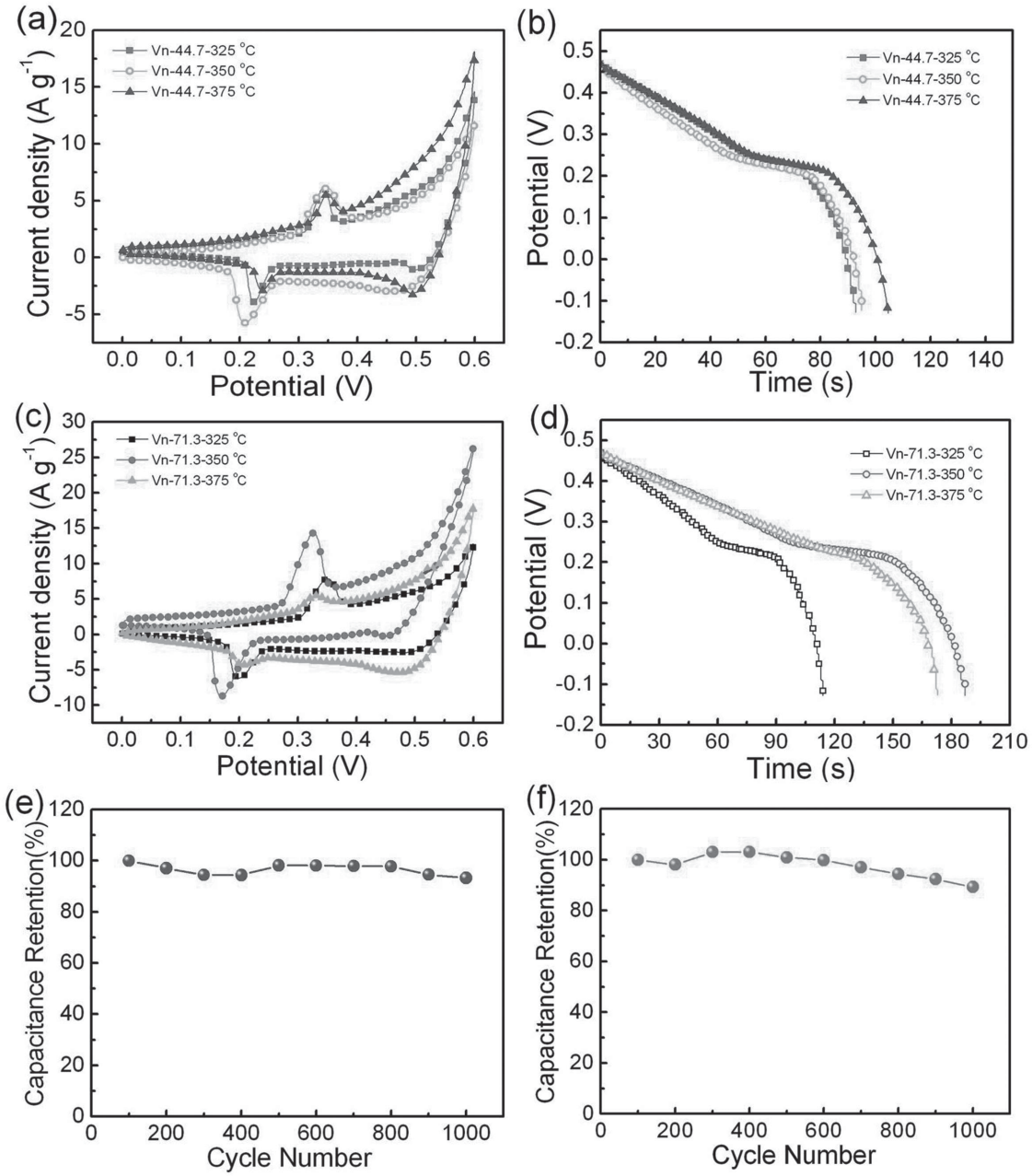

Figure 6. a) Comparison of CV curves at a scan rate of 5 mV s^{-1} for Vn-44.7 samples annealed at different temperatures (325, 350, and 375 °C). b) Comparison of GCD curves at a current density of 2 A g^{-1} for Vn-44.7 samples annealed at different temperatures. c) Comparison of CV curves at a scan rate of 5 mV s^{-1} for Vn-71.3 samples annealed at different temperatures. d) Comparison of GCD curves at a current density of 2 A g^{-1} for Vn-71.3 samples annealed at different temperatures. e) Cycling performance of Vn-44.7–350 °C sample at a current density of 30 A g^{-1}. f) Cycling performance of Vn-71.3–350 °C sample at a current density of 30 A g^{-1}.

curves of the asymmetric supercapacitor measured at various scan rates. Unlike the previously reported sharp redox peaks observed in the CV curves of NiO-based composites,[48–50] the asymmetric supercapacitors show rectangle-like shapes with slight redox peaks in the potential window, indicating typical capacitive behaviors of EDLCs of VACNTs. GCD testing is also performed with different current densities and at a voltage window of 0–1.6 V (Figure 7c). The specific capacitances are calculated based on the total mass of active materials of the positive and negative electrodes. The values of specific capacitance are 255.7, 226.4, 187.5, 137.5, and 70 F g^{-1} at current densities of 1, 2, 3, 5, and 8 A g^{-1}, respectively, as shown in Figure 7d.

Energy density and power density are two important parameters that evaluate the electrochemical performance of the supercapacitors. Based on the GCD curves, the energy density and power density are calculated. Figure 7e depicts the Ragone plot, i.e., power density versus energy density. It shows that the highest energy density of the asymmetric supercapacitor

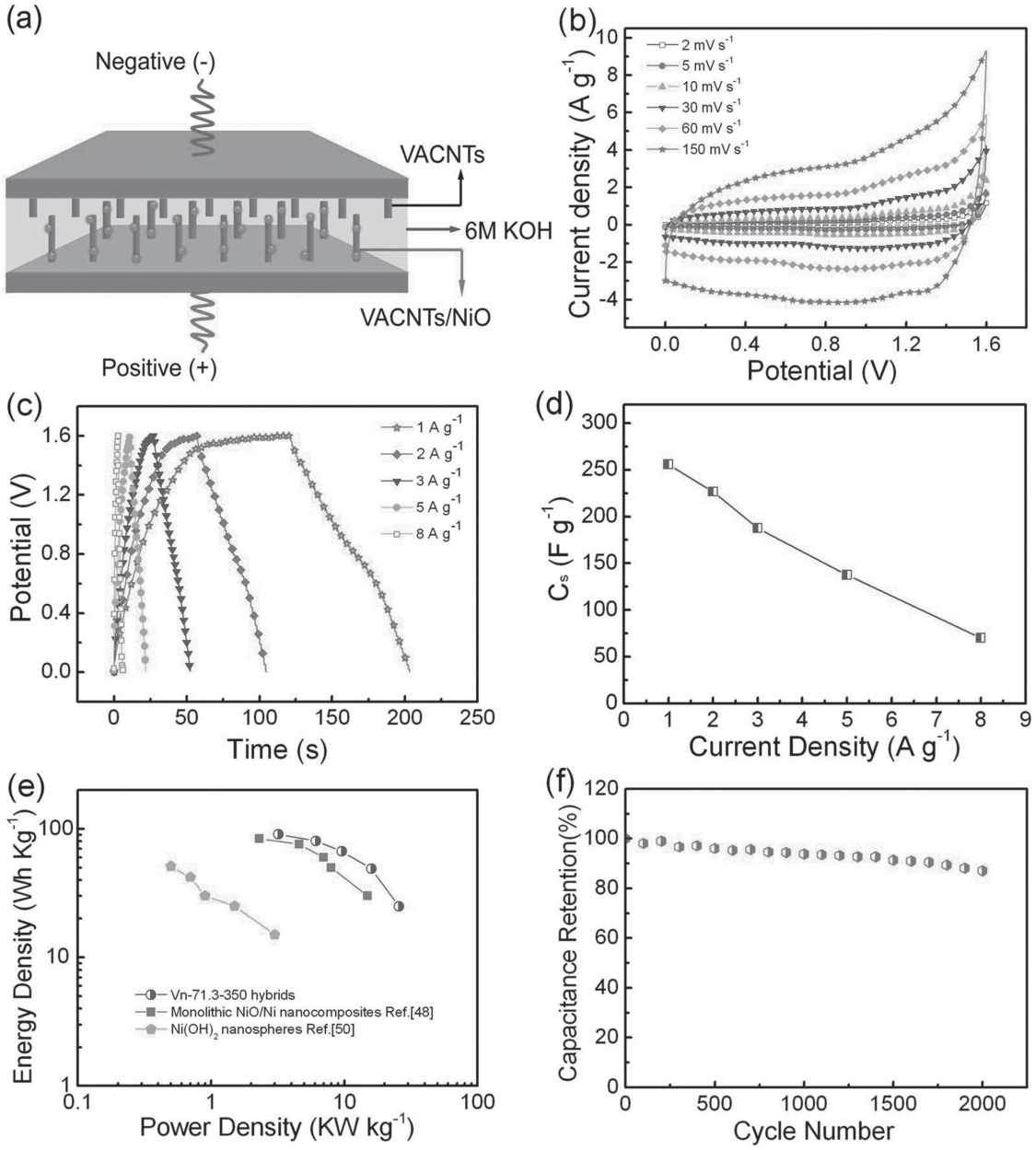

Figure 7. a) Schematic of an asymmetric supercapacitor consisting of VACNTs/NiO and VACNTs electrodes. b) CV curves of the asymmetric supercapacitor at different scan rates. c) Galvanostatic charge–discharge curves and d) corresponding specific capacitance (C_s) of the asymmetric supercapacitor at different current densities. e) Ragone plots (energy density vs power density) of asymmetric supercapacitor consisting of Vn-71.3–350 °C and VACNTs electrodes at different charge–discharge rates, and those of the similar pseudocapacitors reported in the literature.[49,51] f) Cycling performance of the asymmetric supercapacitor at a current density of 5 A g^{-1}.

is 90.9 Wh kg^{-1} at an average power density of 3.2 kW kg^{-1}, the maximum power density is 25.6 kW kg^{-1} at an energy density of 24.9 Wh kg^{-1}. Remarkably, the values of energy density and power density are higher than those of NiO-, VACNT-, or $Ni(OH)_2$-based composite electrodes reported in the literatures.[48–54] Such high energy density of the electrode could be attributed to its high specific capacitance C_s, its much elevated electrochemical window (0–1.6 V) in the aqueous electrolyte, and most importantly, the well assembly of NiO nanoparticles with 3D VACNTs. Furthermore, in most applications of energy storage systems, the stored energy must be released rapidly to meet the power demands, the VACNTs/NiO electrodes with ultrahigh power density are surely more desirable for practical applications.

The GCD measurement is used to evaluate the durability of the as-fabricated asymmetric supercapacitors. As shown in Figure 7f, the as-obtained asymmetric supercapacitors could still retain about 87.1% of its original capacitance even after 2000 cycles at a current density of 5 A g^{-1}, demonstrating the excellent durability of the VACNTs/NiO electrodes.

3. Conclusions

A facile and effective $SCCO_2$-assisted approach is developed to synthesize the VACNTs/NiO hybrid structures. NiO precursors are found to uniformly permeate into the highly dense and ultralong VACNTs with the assistance of $SCCO_2$ fluids. The high-quality VACNTs/NiO hybrid structures are successfully fabricated after annealing. The $SCCO_2$-assisted method can be easily extended to the fabrication of carbon materials or nanostructures decorated with other metal oxide nanoparticles. An ultrahigh specific capacitance of 1088.44 F g^{-1} at a scan rate of 5 mV s^{-1} is achieved in the VACNTs/NiO electrode by optimizing its NiO loading and the annealing temperature. In the asymmetric supercapacitor using VACNTs/NiO hybrids as the positive electrode and the VACNTs as the negative electrode, an energy density of 90.9 Wh kg^{-1} at a power density of 3.2 kW kg^{-1} and a maximum power density of 25.6 KW kg^{-1} at an energy density of 24.9 Wh kg^{-1} could be achieved, which are superior to those reported in the NiO or VACNTs-based asymmetric supercapacitors. After 2000 cycles, the asymmetric supercapacitors could still maintain 87.1% of the initial capacitance.

4. Experimental Section

Synthesis of Vertically Aligned Carbon Nanotube Arrays: The highly dense, millimeter-long VACNTs were synthesized by the water-assisted CVD at 840 °C with high-purity ethylene (99.99%) as carbon source. Si (100) wafers were coated with a buffer layer of 30 nm Al_2O_3 film and a catalyst film of 1.5 nm Fe was used as the substrates. High-purity Ar (99.999%) with H_2 (99.999%) was used as a carrier gas at 1 atm. The total flow rate was 600 sccm. A small and controlled amount of water vapor was introduced to increase catalyst lifetime and was supplied by passing a portion of the Ar carrier gas through a water bubbler. Typical CVD growth was carried out by introducing 100 sccm ethylene and a water concentration of 100–200 ppm at 840 °C for 10 min at ambient pressure. VACNTs with a height of ≈1 mm which consist of nanotubes with diameters of ≈7 nm were grown and utilized for the next step.

Fabrication of VACNTs/NiO Hybrids: In a typical process, VACNTs were first placed in a high-pressure vessel of 50 mL, and the precursor nickelocene organic solution was added dropwise to a container in the vessel. The addition procedure was conducted in a glove box filled with nitrogen gas. Then, the vessel is sealed and connected to the gas pipeline. After the reactor was preheated to 50 °C, CO_2 was slowly introduced by a syringe pump to reach the targeted pressure. Subsequently, the vessel was heated and kept at 100 °C and for 3 h, where the precursor was dissolved into the $SCCO_2$ fluids and adsorbed into the VACNTs. The system was then slowly depressurized and cooled to room temperature. The amount of adsorbed precursor was determined by weighing the VACNTs before and after $SCCO_2$ treatment. The precursor impregnated VACNTs were subsequently transferred to an oven and annealed at various temperatures in air to convert the precursor to nickel oxide.

Characterization: The crystal structures of the products were analyzed using XRD (Advance D8). The morphologies of obtained samples were observed using FE-SEM (Quanta FEG450) and TEM (JEM-2010F, Germany). TGA (Q50, Perkin-Elmer) was carried out in air to determine annealing conditions for the sample and exact loading amount of the oxide. EDS (JEOL-2010) and XPS (PHI 5000C ESCA System) measurements were employed to investigate the compositions of the samples. The atomic structures of the samples were observed by (HRTEM), FEI Tecnai BM-Orius) operated at 200 kV.

Electrochemical Measurement: The electrochemical measurements were carried out in a conventional three-electrode cell with the pure VACNTs or VACNTs/NiO hybrids as the working electrode, a platinum plate as the counter electrode and a saturated calomel as the reference electrode in 6 M KOH aqueous solution. The VACNTs/NiO hybrids were detached from the original substrate by cutting and then directly pressed on nickel mesh to construct the working electrode without using any binders. Cyclic voltammogram (CV), GCD, and EIS measurements were conducted using the CHI750D electrochemical workstation (Shanghai CH Instrument Company, China). The average specific capacitance of the electrodes was calculated from the cyclic voltammograms of the samples according to the equation: $C_s = (q_a + |q_c|)/2 \times m \times \Delta V$, where C_s is the specific capacitance in F g^{-1}, ΔV is the voltage window in V and m (g) is the mass of the active material of the electrode (namely, the mass of VACNT/NiO hybrids). q_a and q_c are the anodic and cathodic charges, respectively, in C. The average specific capacitances were calculated from the GCD curves as follows: $C_s = I \times \Delta t/(\Delta V \times m)$, where C_s (F g^{-1}) is the specific capacitance, I (A) is the discharge current, Δt (s) is the discharge time, ΔV (V) is the potential change during the discharge, and m (g) is the mass of the active material in the electrode. The C_s of asymmetric supercapacitor was calculated from GCD curves as follows: $C_s = 4 \times I \times \Delta t/(\Delta V \times m')$, where m'(g) is the total mass of the active material of the positive and negative electrodes. The energy and power densities of the composites samples, and the asymmetric supercapacitor were calculated as follows: $E = 0.5 \times C \times V^2$, $P_a = E/\Delta t$, where E (Wh kg^{-1}) is the energy density, V (V) is the cell voltage excluding IR drop, P_a (W kg^{-1}) is the average power density, and Δt (s) is the discharge time.

Supporting Information

Supporting Information is available from the Wiley Online Library or from the author.

Acknowledgements

The authors gratefully acknowledge the financial support from the National Natural Science Foundation of China (Grant Nos. 51901086 and 51072118), the Hujiang Foundation of China (B14006), Key Basic Research of Shanghai Science and Technology Program (Grant No. 12JC1406900), and the Science and Technology Innovation Commission of Shenzhen (Grant No. JCYJ2013041152508657). Certain commercial equipment, instruments, or materials are identified in this work. Such identification does not imply recommendation or endorsement by the National Institute of Standards and Technology, nor does it imply that the products identified are necessarily the best available for the purpose.

Received: July 2, 2015
Revised: September 22, 2015
Published online: November 9, 2015

[1] B. E. Conway, *Electrochemical Supercapacitors, Scientific Fundamentals and Technological Applications*, Kluwer Academic, New York, USA **1999**.
[2] P. Simon, Y. Gogotsi, *Nat. Mater.* **2008**, *7*, 845.
[3] P. J. Hall, M. Mirzaeian, S. I. Fletcher, F. B. Sillars, A. J. R. Rennie, G. O. Shitta-Bey, G. Wilson, A. Crude, R. Carterf, *Energy Environ. Sci.* **2010**, *3*, 1238.
[4] H. Jiang, P. S. Lee, C. Z. Li, *Energy Environ. Sci.* **2013**, *6*, 41.
[5] D. N. Futaba, K. Hata, T. Yamada, T. Hiraoka, Y. Hayamizu, Y. Kakudate, O. Tanaike, H. Hatori, M. Yumura, S. Iijima, *Nat. Mater.* **2006**, *5*, 987.
[6] H. Zhang, G. P. Cao, Y. S. Yang, *Energy Environ. Sci.* **2009**, *2*, 932.
[7] Z. Yang, X. M. Zhou, Z. P. Jin, Z. Liu, H. G. Nie, X. A. Chen, S. M. Huang, *Adv. Mater.* **2014**, *26*, 3156.

[8] K. P. Gong, F. Du, Z. H. Xia, M. Durstock, L. M. Dai, *Science* **2009**, *323*, 760.
[9] X. Zhao, B. M. Sanchez, P. J. Dobson, P. S. Grant, *Nanoscale* **2011**, *3*, 839.
[10] X. W. Cui, F. P. Hu, W. F. Wei, W. X. Chen, *Carbon* **2011**, *49*, 1225.
[11] J. W. Long, B. Dunn, D. R. Rolison, H. S. White, *Chem. Rev.* **2004**, *104*, 4463.
[12] Y. Jiang, P. Wang, J. Zhang, W. Li, L. Lin, in*2010 IEEE 23nd Int. Conf. Micro Electro Mechanical Systems*, IEEE, Piscataway, NJ, USA **2010**, p. 1171.
[13] Y. Q. Jiang, P. B. Wang, X. N. Zang, Y. Yang, A. Kozinda, L. W. Lin, *Nano. Lett.* **2013**, *13*, 3524.
[14] J. W. Liu, J. Essner, J. Li, *Chem. Mater.* **2010**, *22*, 5022.
[15] J. Yang, W. D. Zhang, S. Gunasekaran, *Electrochim. Acta* **2011**, *56*, 5538.
[16] I. G. Casella, *J. Electroanal. Chem.* **2002**, *520*, 119.
[17] S. Ma, K. Ahn, E. Lee, K. Oh, K. Kim, *Carbon* **2007**, *45*, 375.
[18] W. Fang, O. Chyan, C. Sun, C. Wu, C. Chen, K. Chen, L. Chen, J. Huang, *Electrochem. Commun.* **2007**, *9*, 239.
[19] L. C. Schumacher, I. B. Holzhueter, I. R. Hill, M. J. Dignam, *Electrochim. Acta* **1990**, *35*, 975.
[20] A. H. Jayatissa, K. Guo, A. C. Jayasuriya, T. Gupta, *Mat. Sci. Eng. B Solid* **2007**, *144*, 69.
[21] H. J. Liu, L. H. Jin, P. He, C. X. Wang, Y. Y. Xia, *Chem. Commun.* **2009**, *44*, 6813.
[22] B. G. Choi, H. Park, T. J. Park, M. H. Yang, J. S. Kim, S. Y. Jang, N. S. Heo, S. Y. Lee, J. Kong, W. H. Hong, *ACS Nano* **2010**, *4*, 2910.
[23] K. W. Nam, K. B. Kim, *J. Electrochem. Soc.* **2002**, *149*, A346.
[24] C. Z. Yuan, B. Gao, X. G. Zhang, *J. Power Sources* **2007**, *173*, 606.
[25] C. Z. Yuan, B. Gao, L. H. Su, X. G. Zhang, *Solid State Ionics* **2008**, *178*, 1859.
[26] K. H. Chang, C. C. Hu, C. Y. Chou, *Chem. Mater.* **2007**, *19*, 2112.
[27] M. T. Lee, C. Y. Fan, Y. C. Wang, H. Y. Li, J. K. Chang, C. M. Tseng, *J. Mater. Chem. A* **2013**, *1*, 3395.
[28] W. K. Schropp, *J. Inorg. Nucl. Chem.* **1962**, *24*, 1688.
[29] N. Saito, Y. Ikushima, T. Goto, *B. Chem. Soc. Jpn.* **1990**, *63*, 1532.
[30] L. Zhang, B. Zhao, X. Y. Wang, Y. X. Liang, H. X. Qiu, G. P. Zheng, J. H. Yang, *Carbon* **2014**, *66*, 11.
[31] B. Zhao, L. Zhang, Y. X. Liang, H. X. Qiu, J. H. Yang, *Appl. Phys. A* **2012**, *108*, 351.
[32] C. Yuan, X. Zhang, L. Su, B. Gao, L. Shen, *J. Mater. Chem.* **2009**, *19*, 5772.
[33] H. Li, D. Yu, Y. Hu, P. Sun, J. Xia, H. Huang, *Carbon* **2010**, *48*, 4547.
[34] P. K. Chu, L. Li, *Mater. Chem. Phys.* **2006**, *96*, 253.
[35] D. S. Dalavi, R. S. Devan, R. S. Patil, Y. R. Ma, P. S. Patil, *Mater. Lett.* **2013**, *90*, 60.
[36] M. C. Biesinger, B. P. Payne, L. W. M. Lau, A. Gerson, R. S. C. Smart, *Surf. Interface Anal.* **2009**, *41*, 324.
[37] S. Talapatra, S. Kar, S. K. Pal, R. Vajtai, L. Ci, P. Victor, *Nat. Nanotechnol.* **2006**, *1*, 112.
[38] R. Shah, X. Zhang, S. Talapatra, *Nanotechnology* **2009**, *20*, 395202.
[39] Y. Honda, T. Haramoto, M. Takeshige, H. Shiozaki, T. Kitamura, M. Ishikawa, *Electrochem. Solid-State Lett.* **2007**, *10*, A106.
[40] Q. Lu, M. W. Lattanzi, Y. Chen, X. Kou, W. Li, X. Fan, K. M. Unruh, J. G. Chen, J. Q. Xiao, *Angew. Chem. Int. Ed.* **2011**, *50*, 6847.
[41] L. Wang, D. L. Wang, *Electrochim. Acta* **2011**, *56*, 5010.
[42] Z. Yang, X. M. Zhou, H. G. Nie, Z. Yao, S. M. Huang, *ACS Appl. Mater. Inter.* **2011**, *3*, 2601.
[43] F. Fievet, P. Germi, F. de Bergevin, M. Figlarz, *J. Appl. Crystallogr.* **1979**, *12*, 387.
[44] W. W. Liu, C. X. Lu, X. L. Wang, K. Liang, B. K. Ta, *Mater. Chem. A* **2015**, *3*, 624.
[45] K. C. Liu, M. A. Anderson, *J. Electrochem. Soc.* **1996**, *143*, 124.
[46] Q. Lu, M. W. Lattanzi, Y. Chen, X. Kou, W. Li, X. Fan, K. M. Unruh, J. G. Chen, J. Q. Xiao, *Angew. Chem. Int. Ed.* **2011**, *50*, 6847.
[47] C. K. Lin, K. H. Chuang, C. Y. Lin, C. Y. Tsay, C. Y. Chen, *Surf. Coat. Technol.* **2007**, *202*, 1272.
[48] H. Wang, H. Yi, X. Chen, X. Wang, *J. Mater. Chem. A* **2014**, *2*, 3223.
[49] Q. Lu, M. W. Lattanzi, Y. Chen, X. Kou, W. Li, X. Fan, K. M. Unruh, J. G. Chen, J. Q. Xiao, *Angew. Chem. Int. Ed.* **2011**, *50*, 6847.
[50] C. D. Wang, J. L. Xu, M. F. Yuen, J. Zhang, Y. Y. Li, X. F. Chen, W. J. Zhang, *Adv. Funct. Mater.* **2014**, *24*, 6372.
[51] H. B. Li, M. H. Yu, F. X. Wang, P. Liu, Y. Liang, J. Xiao, C. X. Wang, Y. X. Tong, G. W. Yang, *Nat. Commun.* **2013**, *4*, 1894.
[52] K. Liang, X. Tang, W. Hu, *J. Mater. Chem.* **2012**, *22*, 11062.
[53] X. Lu, D. Zheng, T. Zhai, Z. Liu, Y. Huang, S. Xie, Y. Tong, *Energy Environ. Sci.* **2011**, *4*, 2915.
[54] Y. C. Qiu, G. Z. Li, Y. Hou, Z. H. Pan, H. F. Li, W. F. Li, M. N. Liu, F. M. Ye, X. W. Yang, Y. G. Zhang, *Chem. Mater.* **2015**, *27*, 1194.